Research Article Vol. 34, No. 5 / 9 Mar 2026 / Optics Express 8506
Optics EXPRESS

Adaptive orthogonal matching pursuit and group K-SVD dictionary learning framework for bioluminescence tomography

BIANBIAN YANG,[1] XIN ZHOU,[1] JIAXIN DU,[1] YI CHEN,[1,2,4] HUANGJIAN YI,[1] LINZHI SU,[1,5] CHENGYI GAO,[3] AND XIN CAO[1,6]

[1]College of Computer Science, Northwest University, Xi'an, Shaanxi 710127, China
[2]School of Electrical and Mechanical Engineering, The University of Adelaide, Adelaide, SA 5005, Australia
[3]Department of Oncology, The First Affiliated Hospital, Xi'an Jiaotong University, Xi'an, Shaanxi 710061, China
[4]yichen.cgz@gmail.com
[5]sulinzhi029@163.com
[6]caoxin918@hotmail.com

Abstract: Bioluminescence tomography (BLT) is a promising molecular imaging modality with significant potential in preclinical research, enabling three-dimensional quantitative reconstruction of internal bioluminescent sources. However, the low absorption and severe photon scattering effects in biological tissues render the BLT inverse problem highly ill-conditioned, often leading to unstable and inaccurate reconstruction results. In this study, an adaptive orthogonal matching pursuit with group K-singular value decomposition (AOMP-GKSVD) algorithm is proposed within a dictionary learning framework. An adaptive sparsity estimation mechanism is incorporated into the sparse coding phase to infer the sparsity level from the measured data and the system matrix, thereby better capturing the intrinsic sparsity characteristics of bioluminescent sources. This overcomes the limitation of fixed sparsity settings in conventional OMP, enhancing reconstruction accuracy and robustness, while saving time and effort by eliminating the need for manual sparsity tuning under varying noise and source conditions. During the dictionary update phase, a grouping strategy based on a discretized tetrahedral mesh is employed, in which atoms are updated collectively at the group level, exploiting spatial adjacency to maintain coherence and efficiently reconstruct clustered source regions. The performance of AOMP-GKSVD was validated through a series of numerical simulations and a light source implantation experiment. The experimental results demonstrate that AOMP-GKSVD achieves superior performance in terms of localization accuracy, morphological recovery, and robustness, highlighting its potential to advance the practical application of BLT in preclinical optical molecular imaging.

1. Introduction

Bioluminescence imaging (BLI) is a non-invasive and highly sensitive optical molecular imaging modality capable of visualizing luciferase-labeled tumor cells *in vivo* [1, 2]. Owing to its exceptional sensitivity, BLI has become an indispensable tool in preclinical research, particularly for tumor monitoring, drug development, and the investigation of cellular and molecular mechanisms [3, 4]. However, BLI only captures the two-dimensional (2D) photon distribution emitted from the body surface, which is insufficient for accurately localizing or quantifying the three-dimensional (3D) spatial distribution of internal bioluminescent sources [5, 6].

To overcome this fundamental limitation, bioluminescence tomography (BLT) has been developed as a 3D extension of BLI [7]. By integrating surface photon flux measurements with the forward light propagation model and inverse reconstruction algorithms, BLT enables the

#587324 https://doi.org/10.1364/OE.587324
Journal © 2026 Received 9 Dec 2025; revised 24 Jan 2026; accepted 9 Feb 2026; published 2 Mar 2026

Optics EXPRESS

recovery of the 3D spatial distribution of internal bioluminescent sources [8]. This 3D visualization and quantification capability has significantly broadened its applications in preclinical studies, including glioma imaging [9], breast cancer monitoring [10], and *in vivo* stem cell tracking [11]. Nevertheless, BLT reconstruction remains a challenging and severely ill-posed inverse problem. The propagation of bioluminescent photons is strongly affected by scattering and absorption within biological tissues, and the number of surface measurements is typically far less than the number of unknown variables in the source distribution [12, 13]. These factors inherently limit the stability and accuracy of the BLT reconstruction [14]. Consequently, developing effective reconstruction strategies to mitigate this ill-posedness and improve reconstruction accuracy remains a critical research focus in optical molecular imaging [15].

Numerous approaches have been proposed to address the BLT reconstruction challenge, which can be broadly categorized into deep learning-based methods and classical mathematical iterative methods [16]. Deep learning-based approaches offer substantial flexibility and automated feature extraction capabilities, achieving high tumor localization accuracy in both simulated and experimental studies [17]. For example, Rezaeifar et al. demonstrated sub-millimeter localization precision and a high Dice similarity coefficient (DSC) in BLT experiments [18]. However, these methods often suffer from poor interpretability and a heavy reliance on large, high-quality datasets, which constrain their generalization and practical applicability [19]. As a result, mathematically interpretable and data-efficient optimization frameworks continue to be a major research focus for BLT reconstruction.

Within mathematical iterative approaches, regularization-based methods introduce penalty terms such as the L_1-norm [20] and L_2-norm [21] to stabilize the ill-posed inverse problem, but they may produce over-sparse or over-smoothed results [22]. To better balance sparsity and fidelity, nonconvex sparse regularization (NSR) penalties, such as the smoothly clipped absolute deviation (SCAD) [23] and minimax concave penalty (MCP) [24], have been proposed. Nevertheless, their lack of explicit structural priors limits their ability to recover accurate source morphologies [25]. To overcome these limitations, Bayesian models offer an alternative by incorporating statistical priors and uncertainty modeling to capture spatial correlations and enhance structural coherence. For instance, Gaussian Markov random field (GMRF) priors are employed to preserve source boundaries, while Laplace and Gaussian priors impose sparsity or smoothness constraints [26, 27]. However, their high computational cost and reliance on carefully designed priors often limit their scalability [28]. While algorithms like the alternating direction method of multipliers (ADMM) [29] and the fast iterative shrinkage-thresholding algorithm (FISTA) [30] provide stable convergence for iterative optimization, greedy methods such as orthogonal matching pursuit (OMP) [31] offer faster computation but rely on a manually predefined sparsity level, which limits adaptability and reduces robustness [32]. In parallel, dictionary learning algorithms have been widely applied in image processing [33], compressed sensing [34], and optical molecular imaging [35]. Among them, the K-singular value decomposition (K-SVD) method [36] alternates between sparse coding and dictionary update stages to iteratively refine data representations. Although K-SVD enhances reconstruction accuracy and flexibility, its conventional column-by-column update scheme fails to exploit the inherent spatial correlations among neighboring nodes, thereby limiting its ability to recover spatially clustered sources and preserve structural consistency [37, 38].

In this paper, an adaptive OMP with group K-SVD (AOMP-GKSVD) algorithm within a dictionary learning framework is proposed to enhance the sparse reconstruction of clustered bioluminescent sources. In the sparse coding stage, the sparsity level is adaptively inferred from the measurement data and the system matrix, overcoming the reliance on a fixed and empirically chosen sparsity level in conventional OMP [34]. This data-driven inference mechanism allows the algorithm to self-adjust its sparse representation based on the intrinsic structure of the measurement data, thereby improving reconstruction accuracy while eliminating the need for

Optics EXPRESS

manual parameter tuning. Additionally, atom selection is performed at the node level, enabling fine-grained spatial precision in identifying active source locations. During the dictionary update stage, a group-structured K-SVD strategy is introduced. Based on the finite element discretization, adjacent vertex nodes of each tetrahedral element form overlapping spatial groups [32]. Unlike in traditional K-SVD, dictionary atoms within each group are jointly optimized, enabling the model to capture local spatial correlations and enforce structural coherence. By integrating adaptive sparsity estimation with group-structured dictionary updates, the AOMP-GKSVD framework transforms the classical OMP-KSVD algorithm into a data-driven, structure-aware method, achieving robust, high-fidelity, and spatially coherent reconstructions. To evaluate the performance of our proposed method, two numerical simulations and a light source implantation experiment were carried out. Four representative algorithms were selected for comparison to assess localization accuracy, morphological recovery, and robustness: the incomplete variables truncated conjugate gradient algorithm with L_1 regularization (IVTCG-L_1) [14], FISTA with L_1 regularization (FISTA-L_1) [30], the regularized smoothed L_0-norm (ReSL0) algorithm [39], and the conventional OMP-KSVD algorithm [36].

The remainder of this paper is organized as follows. Section 2 presents the BLT forward model, formulates the inverse problem, and details the proposed AOMP-GKSVD method. Section 3 introduces the evaluation metrics and describes the setup for numerical simulations and the light source implantation experiment. Section 4 presents the 3D reconstruction results, including comparative and quantitative analyses. Finally, Section 5 discusses and concludes the main findings of this work.

2. Methodology

2.1. Traditional numerical model method for BLT reconstruction

The propagation of light in biological tissue is rigorously governed by the Radiative Transfer Equation (RTE) [40]. However, solving the RTE numerically is computationally demanding, particularly for applications involving complex geometries and highly anisotropic photon transport [41]. To overcome this challenge, several approximate models have been proposed, among which the Diffusion Equation (DE) is the most widely adopted in BLT reconstruction. As a first-order approximation of the RTE, the DE captures the essential characteristics of photon transport while providing a computationally efficient and sufficiently accurate description in homogeneous or weakly heterogeneous tissues [4, 5].

To ensure the validity of the diffusion approximation, BLT experiments are typically conducted in a strictly controlled, light-free environment to eliminate external light interference [5]. To account for the refractive-index mismatch at the tissue-air interface, which causes partial internal reflection and refraction of photons, a Robin-type boundary condition is imposed [42]. The steady-state DE with this boundary condition can be expressed as follows:

$$\begin{cases} -\nabla \cdot [D(r)\nabla\phi(r)] + \mu_a(r)\phi(r) = S(r), r \in \Omega \\ \phi(r) + 2A(n)D(r)[\boldsymbol{\nu}(\boldsymbol{r}) \cdot \nabla\phi(r)] = 0, r \in \partial\Omega \end{cases} \tag{1}$$

where $S(r)$ denotes the internal bioluminescent source intensity distribution, $\phi(r)$ is the photon flux density, Ω represents the tissue domain, and $\partial\Omega$ is the boundary region of Ω. $\boldsymbol{\nu}$ is the outward normal vector on the boundary, and n is the tissue refractive index. The diffusion coefficient at position r is given by $D(r) = \frac{1}{3[\mu_a(r)+(1-g)\mu_s(r)]}$, where $\mu_a(r)$ and $\mu_s(r)$ are the absorption and scattering coefficients, respectively, and g is the anisotropy factor. $A(n)$ represents the refractive index mismatch factor at the tissue-air interface and is defined as:

$$A(n) = \frac{1 + (1.4399n^{-2} + 0.7099n^{-1} + 0.6681 + 0.636n)}{1 - (1.4399n^{-2} + 0.7099n^{-1} + 0.6681 + 0.636n)} \tag{2}$$

Optics EXPRESS

Based on the Robin-type boundary condition, the theoretical value of the photon flux density on the surface of the biological tissue can be expressed as:

$$\Gamma(r) = -D(r)[\boldsymbol{v}(\boldsymbol{r}) \cdot \nabla\phi(r)] = \phi(r)/2A(n) \tag{3}$$

Owing to the irregular geometry of biological tissues, the finite element method (FEM) is employed to discretize the photon propagation model. This discretization yields a system of linear equations that serves as the forward model, linking the measured surface photon flux to the internal bioluminescent source distribution [43].

$$\boldsymbol{AX} = \boldsymbol{\Phi} \tag{4}$$

where $\boldsymbol{A} \in \mathbb{R}^{m\times n}$ denotes the system matrix encoding the optical properties of each tissue region, $\boldsymbol{\Phi} \in \mathbb{R}^{m\times 1}$ represents the measured photon flux on the tissue boundary, and $\boldsymbol{X} \in \mathbb{R}^{n\times 1}$ denotes the unknown internal bioluminescent source distribution.

2.2. Reconstruction based on AOMP-GKSVD method

Reconstructing $\boldsymbol{X}$ from surface photon flux measurements $\boldsymbol{\Phi}$ in Eq. (4) is severely ill-posed, since strong scattering and absorption in biological tissue make the forward mapping intrinsically smoothing and the system matrix $\boldsymbol{A}$ ill-conditioned, rendering the inversion highly sensitive to noise and modeling errors [25, 27]. Therefore, prior information is required to obtain stable and physically meaningful reconstructions [26].

Motivated by the sparsity and spatially localized support of BLT sources, we formulate Eq. (4) from a sparse representation perspective, where $\boldsymbol{A}$ can be regarded as an overcomplete dictionary and $\boldsymbol{X}$ denotes the corresponding sparse coefficient vector [12–14]. To enhance reconstruction accuracy and stability, the AOMP-GKSVD algorithm is developed within a dictionary learning framework. Specifically, the proposed method integrates an adaptive sparsity estimation strategy into the OMP process for sparse coding and adopts a grouping strategy based on tetrahedral elements for dictionary updating [32, 34]. By combining adaptive sparse coding with dictionary updating within groups, the approach effectively preserves local spatial structures, enhances spatial coherence, and improves computational robustness. The overall framework comprises three major stages: adaptive sparse coding, spatial grouping, and dictionary updating within groups.

Conventional sparse reconstruction under this formulation typically employs L_1 regularization to promote sparsity, expressed as:

$$\min_{\boldsymbol{X}} F(\boldsymbol{X}) = \frac{1}{2}||\boldsymbol{AX} - \boldsymbol{\Phi}||_2^2 + \lambda||\boldsymbol{X}||_1 \tag{5}$$

where λ is the regularization parameter that balances data fidelity and sparsity. The corresponding basis pursuit form of the problem can be written as:

$$min||\boldsymbol{X}||_1 \quad s.t.\ \boldsymbol{AX} = \boldsymbol{\Phi} \tag{6}$$

2.2.1. Adaptive sparse coding stage

To achieve stable and accurate sparse representations, an AOMP algorithm incorporates an adaptive sparsity estimation strategy into the traditional OMP framework. The primary objective is to improve reconstruction accuracy and robustness in BLT by overcoming the limitations of fixed sparsity levels in standard OMP.

Optics EXPRESS

Adaptive sparsity estimation Conventional OMP requires a manually predefined sparsity level K, which is typically determined empirically. However, in BLT reconstruction, the true sparsity of bioluminescent sources may vary significantly among samples due to tissue heterogeneity and differences in optical absorption [32]. Consequently, using a fixed K may lead to over-sparse or under-sparse representations, thereby compromising reconstruction quality.

To address this issue, a projection-correlation criterion is employed to adaptively estimate the sparsity level $\widehat{K}_l$ by searching for the smallest integer K satisfying the criterion [34]. For the l-th measurement vector $\boldsymbol{\Phi}_l$, its correlation with the system matrix $\boldsymbol{A}$ is first computed, and the K most correlated atoms are selected to form the candidate support set $\Gamma_{(K)}$. The sparsity level is then determined as:

$$\widehat{K}_l = \min_K \left\{ K \mid \left|\left|\boldsymbol{A}_{\Gamma_{(K)}}^T \boldsymbol{\Phi}_l\right|\right|_2 < \frac{1-\delta}{\sqrt{1+\delta}} ||\boldsymbol{\Phi}_l||_2 \right\} \tag{7}$$

where δ is a predefined projection-correlation threshold controlling the stringency of the test in Eq. (7). Starting from $K = 1$, we increment K until Eq. (7) is satisfied, and the first K that satisfies Eq. (7) is taken as the estimated sparsity $\widehat{K}_l$. With the columns of A normalized to unit L_2-norm, the obtained $\widehat{K}_l$ is then used as the sparsity input for the subsequent OMP pursuit stage.

OMP with adaptive sparsity Given the estimated sparsity level $\widehat{K}_l$, the OMP algorithm proceeds as a greedy pursuit method to obtain the sparse representation. An empty support set S is initialized. At each iteration, the correlation between the residual vector r^{k-1} and each column $\boldsymbol{A}_i$ of the system matrix is computed, and the atom with the maximum correlation S_k is selected and added to the support set S, as formulated in Eq. (8):

$$\begin{aligned} S_k &= \underset{i}{argmax} \, ||\boldsymbol{A}_i{}^T r^{k-1}||_1 \\ S &= S \cup S_k \end{aligned} \tag{8}$$

where k denotes the current iteration. The residual vector r^k is updated by subtracting the projection of the measurement vector $\boldsymbol{\Phi}$ onto the subspace spanned by the columns of the current support matrix $\boldsymbol{A}_S$:

$$r^k = \boldsymbol{\Phi} - proj(\boldsymbol{\Phi}, \boldsymbol{A}_S) = \boldsymbol{\Phi} - \boldsymbol{A}_S \boldsymbol{A}_S{}^+ \boldsymbol{\Phi} \tag{9}$$

where $\boldsymbol{A}_S{}^+$ denotes the pseudo-inverse of the submatrix $\boldsymbol{A}_S$, calculated as:

$$\boldsymbol{A}_S{}^+ = (\boldsymbol{A}_S{}^T \boldsymbol{A}_S)^{-1} \boldsymbol{A}_S{}^T \tag{10}$$

Once the support set S is determined, the nonzero coefficients of the sparse vector $\boldsymbol{X}$ are obtained by:

$$\boldsymbol{X}_S = \boldsymbol{A}_S{}^+ \boldsymbol{\Phi} \tag{11}$$

The coefficient vector $\boldsymbol{X}$ is initialized as a zero vector, and during each iteration, only the entries corresponding to the current support set are updated, ensuring that the reconstruction is constrained to the selected atoms.

2.2.2. Grouping stage

In BLT, bioluminescent sources typically appear as localized clusters rather than isolated points. To capture this spatial characteristic, a grouping strategy based on the adjacency of tetrahedral elements is employed during the dictionary update phase within the finite element framework. Specifically, the reconstruction domain is discretized into tetrahedral elements, and the four adjacent nodes of each element are treated as a single group [32]. This strategy preserves local spatial correlations and reflects the clustered distribution of bioluminescent sources, thereby enhancing spatial coherence, structural consistency, and reconstruction robustness [44].

Optics EXPRESS

To explicitly incorporate this spatial structure into the reconstruction, groups are defined based on the tetrahedral elements:

$$G_m = \{v_{m1}, v_{m2}, v_{m3}, v_{m4}\},\ m = 1, 2, \cdots, N_t \tag{12}$$

where N_t denotes the total number of tetrahedral elements, corresponding to the total number of groups.

Under this grouping scheme, the reconstruction coefficient vector $\boldsymbol{X}$ can be expressed as:

$$\boldsymbol{X} = (\boldsymbol{X}_{G_1}, \boldsymbol{X}_{G_2}, \cdots \boldsymbol{X}_{G_{N_t}})^T \tag{13}$$

where $\boldsymbol{X}_{G_m}$ contains the coefficients associated with the nodes in the group G_m. Similarly, the boundary photon flux vector $\boldsymbol{\Phi}$ can be represented as:

$$\boldsymbol{\Phi} = (\boldsymbol{\Phi}_{G_1}, \boldsymbol{\Phi}_{G_2}, \cdots \boldsymbol{\Phi}_{G_{N_t}})^T \tag{14}$$

This grouping strategy is incorporated into the dictionary update stage of the K-SVD algorithm. By integrating local geometric information from the tetrahedral mesh, it preserves spatial adjacency among neighboring nodes and enhances both the robustness and efficiency of the reconstruction process.

2.2.3. Dictionary update within groups

Building upon the previously defined grouping scheme, the dictionary is updated using a Group-KSVD algorithm, which extends the conventional K-SVD framework by performing atom updates guided by the tetrahedral structure of the reconstruction domain.

The optimization problem can be formulated as:

$$\min_{\boldsymbol{A}} ||\boldsymbol{A}\boldsymbol{X} - \boldsymbol{\Phi}||_2^2 \quad s.t. ||\boldsymbol{A}_{:,j}||_2 = 1, \forall j \tag{15}$$

where each column $\boldsymbol{A}_{:,j}$ represents a normalized dictionary atom (basis vector), and each row of $\boldsymbol{X}$ contains the corresponding sparse coefficients. The normalization constraint $||\boldsymbol{A}_{:,j}||_2 = 1$ prevents unbounded scaling during dictionary learning.

Following the standard K-SVD update rule, Eq. (15) can be reformulated as:

$$\underset{\boldsymbol{A}}{argmin} \left\| \boldsymbol{\Phi} - \sum_{j \neq i} \boldsymbol{A}_j \boldsymbol{X}_j^T - \boldsymbol{A}_i \boldsymbol{X}_i^T \right\|_2^2 \tag{16}$$

where $\boldsymbol{A}_j$ denotes the j-th atom and $\boldsymbol{X}_j^T$ is the corresponding row of sparse coefficients.

For the group of atoms G_m corresponding to the m-th tetrahedral element, the group residual matrix is defined as:

$$E_{G_m} = \boldsymbol{\Phi} - \sum_{j \notin G_m} \boldsymbol{A}_j \boldsymbol{X}_j^T \tag{17}$$

Applying SVD to the group residual yields:

$$E_{G_m} = U \Sigma V^T \tag{18}$$

The dictionary atoms and coefficients within the group G_m are then jointly updated by retaining the top r singular components, where r is typically 1 or equal to the rank of $\boldsymbol{X}_{G_m}$:

$$\begin{aligned} \boldsymbol{A}_{G_m} &= U_{:,1:r} \\ \boldsymbol{X}_{G_m} &= \Sigma_{1:r,1:r} V_{:,1:r}^T \end{aligned} \tag{19}$$

By updating dictionary atoms at the group level, the proposed Group-KSVD integrates geometric priors from the tetrahedral mesh and enables correlated atoms to be updated simultaneously. This strategy preserves spatial coherence, enhances structural fidelity, and mitigates

Optics EXPRESS

the limitations of conventional K-SVD updates that disregard local spatial correlations, thereby improving reconstruction robustness, particularly when neighboring sources exhibit correlated spatial distributions.

The AOMP-GKSVD algorithm is outlined in Algorithm 1.

Algorithm 1. AOMP-GKSVD algorithm for BLT reconstruction.

Input: system matrix $\boldsymbol{A}\epsilon\mathbb{R}^{m\times n}$, photon measurement $\boldsymbol{\Phi}\epsilon\mathbb{R}^{m\times 1}$, node coordinates Nodes.
Initialization: support set $I=\emptyset$, residual error vector $r^0=\boldsymbol{\Phi}$, $\boldsymbol{X}^{(0)}\epsilon\mathbb{R}^{n\times 1}$, and $\boldsymbol{A}^{(0)}\epsilon\mathbb{R}^{m\times n}$ with each column normalized to unit L_2-norm, sparsity parameter $\delta=1\mathrm{e}-3$, $err=1e-6$, $iter=0$.
While $||\boldsymbol{X}^{(i)}-\boldsymbol{X}^{(i-1)}||_2 > err$ or $iter < maxIter$ do
  Step1: Adaptive sparse coding
    1) Estimate adaptive sparsity $\widehat{K_l}$ via Eq. (7).
    2) Update sparse coefficients $\boldsymbol{X}$ using adaptive OMP through the Eq. (8), Eq. (9), Eq. (10), Eq. (11).
  Step2: Dictionary Update Within Groups
    For each tetrahedral group G_m defined in Eq. (12):
    1) Compute group residual matrix E_{G_m} through the Eq. (17).
    2) Perform SVD on E_{G_m} through the Eq. (18).
    3) Update dictionary atoms $\boldsymbol{A}_{G_m}$ and coefficients $\boldsymbol{X}_{G_m}$ using top r singular values through the Eq. (19).
  Step3: $iter=iter+1$
End while
Output: $\boldsymbol{X}=\boldsymbol{X}^{(i+1)}$

3. Experiment design

To validate the performance of the proposed AOMP-GKSVD algorithm, a series of numerical simulations and an *in vivo* experiment were conducted. The reconstruction results were compared with four representative algorithms: IVTCG-L_1, FISTA-L_1, ReSL0, and OMP-KSVD. Key performance metrics were systematically evaluated, including localization accuracy, morphological recovery, contrast-to-noise performance, and robustness to noise. All computations and experiments were executed on a laptop with an AMD Ryzen 7 3700U CPU (2.30 GHz), Radeon Vega Mobile Gfx, and 8GB of RAM.

3.1. Evaluation metrics

Four metrics were employed to quantitatively evaluate reconstruction performance: localization error (LE), Dice similarity coefficient (DICE), contrast-to-noise ratio (CNR), and runtime (Time) [7]. LE measures the accuracy of source localization by calculating the Euclidean distance between the center of the reconstructed source $(x_r,\ y_r,\ z_r)$ and the true source $(x_t,\ y_t,\ z_t)$:

$$LE=\sqrt{(x_r-x_t)^2+(y_r-y_t)^2+(z_r-z_t)^2} \tag{20}$$

A smaller LE value signifies higher localization accuracy.

DICE quantifies the morphological recovery by evaluating the volumetric overlap between the reconstructed region R_r and the true region R_t:

$$DICE=2\frac{|R_r\cap R_t|}{|R_r|+|R_t|} \tag{21}$$

Optics EXPRESS

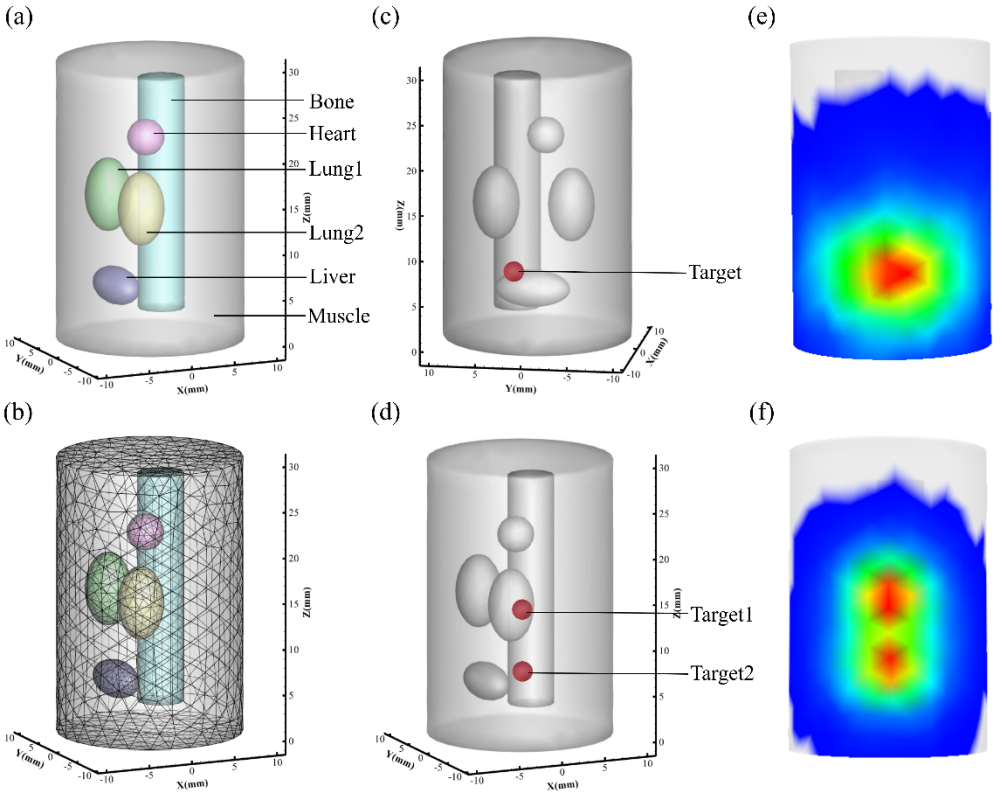

Fig. 1. Heterogeneous cylindrical phantom for numerical simulations: (a) 3D schematic of the cylindrical phantom. (b) 3D view of the tetrahedral finite element mesh. (c) Phantom model with single-source. (d) Phantom model with dual-source. (e) Surface photon distribution from forward simulation with single-source. (f) Surface photon distribution from forward simulation with dual-source.

The DICE index ranges from 0 to 1, with a higher value indicating better morphological recovery of the source.

CNR evaluates contrast recovery relative to noise and is defined as:

$$CNR = \frac{|\mu_{ROI} - \mu_{BCK}|}{\sqrt{m_{ROI}\sigma_{ROI}^2 + m_{BCK}\sigma_{BCK}^2}} \tag{22}$$

where μ_{ROI} and μ_{BCK} are the mean reconstructed values within the region of interest (ROI) and background (BCK), respectively; σ_{ROI}^2 and σ_{BCK}^2 are the corresponding variances; and m_{ROI} and m_{BCK} denote the numbers of mesh nodes within the ROI and background. A larger CNR indicates higher contrast relative to noise and thus better reconstruction quality.

3.2. Numerical simulation experiments setup

A heterogeneous cylindrical phantom with a radius of 10 *mm* and a height of 30 *mm* was constructed for numerical simulations, as illustrated in Fig. 1(a). The phantom contained five major organs: muscle, bone, heart, liver, and lung. The optical properties of each tissue type at a wavelength of 650 *nm*, including the absorption and scattering coefficients and the anisotropy factor, are summarized in Table 1 [38, 45]. The phantom was discretized into a finite element mesh consisting of 4,626 nodes and 25,840 tetrahedral elements using COMSOL Multiphysics

Optics EXPRESS

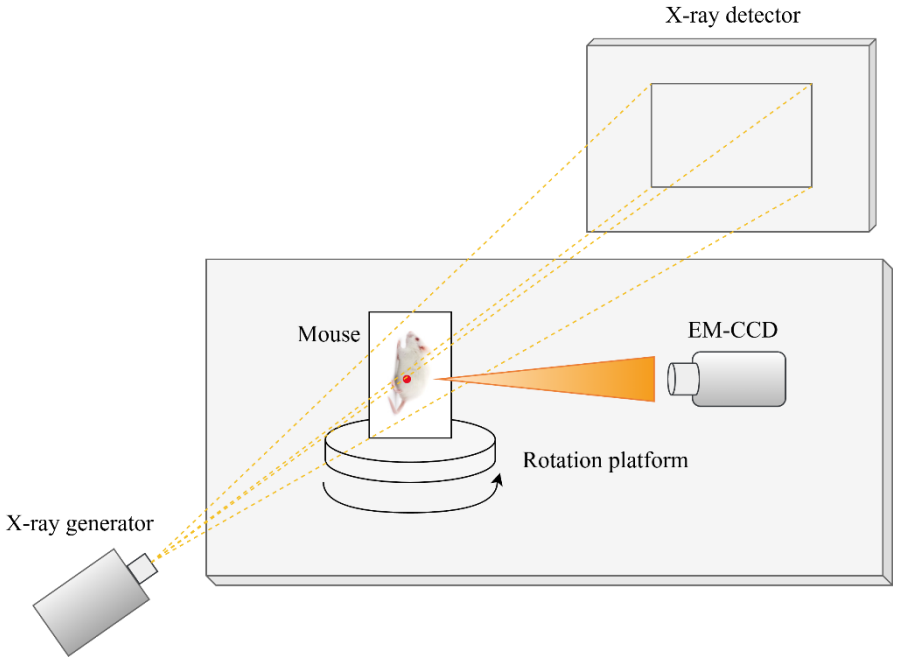

Fig. 2. Schematic diagram of the BLT/CT dual-modality imaging system.

5.6 (COMSOL, Inc., Burlington, Massachusetts) [46], as shown in Fig. 1(b). Forward simulations were conducted using the Monte Carlo method implemented in the molecular optical simulation environment (MOSE, Version 2.3), with results presented in Fig. 1(e) and Fig. 1(f) [47].

Table 1. Optical parameters used for the heterogeneous cylindrical phantom at 650 nm.

Tissue	$\mu_a(r)[mm^{-1}]$	$\mu_s(r)[mm^{-1}]$	g
Muscle	0.0052	10.80	0.900
Bone	0.0060	60.09	0.900
Heart	0.0083	6.733	0.850
Liver	0.0329	7.000	0.900
Lung	0.0133	19.70	0.900

Three simulation scenarios were designed to evaluate the reconstruction algorithms. In the single-source simulation, a spherical light source with a radius of 1 *mm* was positioned at (−6, 2, 8) *mm* within the phantom, as shown in Fig. 1(c). The dual-source simulation involved two identical spherical sources located at (−3, −7, 8.5) *mm* and (−3, −7, 15) *mm* to assess the ability to resolve multiple targets, as displayed in Fig. 1(d). To quantify the robustness of the AOMP-GKSVD algorithm against noise, Gaussian noise with intensity levels of 5%, 10%, 15%, 20%, 25%, and 30% was added to the single-source measurement data.

3.3. *Light source implantation experiment setup*

To further assess the practical feasibility of the AOMP-GKSVD method for *in vivo* BLT reconstruction, a light source implantation experiment was conducted on a female BALB/c nude mouse (6-8 weeks old) using a dual-modality BLT/CT imaging system, as shown in Fig. 2. The mouse was anesthetized with a 3% isoflurane-air mixture and immobilized on a motorized

Optics EXPRESS

rotation stage to minimize motion artifacts during data acquisition. A small, flexible plastic tube with a radius of 1 *mm* and a height of 2 *mm* was surgically implanted into the abdominal region at coordinates (6, 12, 20) *mm* to serve as a surrogate for a bioluminescent source. Bioluminescent signals were captured using an electron multiplying charge-coupled device (EMCCD) camera (iXonEM + 888, −80°C) equipped with a 630 *nm* band-pass filter and a 1 *s* exposure time. Anatomical data were acquired using the integrated CT unit of the BLT/CT system with a tube voltage of 50 kVp and an X-ray power of 40 W.

Following data acquisition, a landmark-based rigid registration method was applied to align the bioluminescence images with the CT data. The 2D surface photon distribution was subsequently projected onto the 3D surface mesh of the mouse model. Major organs, including muscle, heart, lung, liver, stomach, and kidney, were segmented from the CT data using Amira 5.2 (Visage Imaging, Australia). For the final reconstruction, the mouse model was discretized into 6,848 nodes and 38,468 tetrahedral elements.

4. Results

4.1. Numerical simulations results

4.1.1. Single-source reconstruction

The reconstruction performance of the five algorithms is shown in Fig. 3 for the single-source experiment. From left to right, the columns correspond to FISTA, IVTCG, ReSL0, OMP-KSVD, and AOMP-GKSVD. The top row presents the 3D reconstructions, where the reconstructed source is highlighted in red. The bottom row shows the corresponding cross-sectional views at the plane $X = -6$ *mm*, with the white circle indicating the true location and boundary of the implanted target. The quantitative results in Table 2 confirm that AOMP-GKSVD outperforms the other methods in terms of localization accuracy, morphological recovery, and contrast-to-noise performance. Specifically, AOMP-GKSVD achieves the lowest LE of 0.258 *mm*, the highest DICE of 0.760, and the highest CNR of 0.891. In comparison, FISTA, IVTCG, ReSL0, and OMP-KSVD yield larger LE values of 1.246, 0.522, 0.432, and 0.362 *mm*, respectively, along with lower DICE values of 0.480, 0.491, 0.469, and 0.502 and lower CNR values of 0.129, 0.221, 0.328, and 0.430. In addition, AOMP-GKSVD is substantially faster than FISTA, ReSL0, and OMP-KSVD, while its runtime remains only marginally higher than that of IVTCG. These results demonstrate that AOMP-GKSVD provides a more accurate and reliable reconstruction of the single bioluminescent source.

Table 2. Quantitative results of different methods in single-target reconstruction experiment.

Method	Reconstructed results (*mm*)	LE (*mm*)	DICE	CNR	Time (*s*)
FISTA-L_1	(−5.006, 2.474, 7.418)	1.246	0.480	0.129	64.635
IVTCG-L_1	(−6.268, 2.091, 7.561)	0.522	0.491	0.221	45.680
ReSL0	(−6.312, 1.828, 7.757)	0.432	0.469	0.328	48.471
OMP-KSVD	(−5.714, 1.879, 7.815)	0.362	0.502	0.430	49.661
AOMP-GKSVD	(−5.916, 2.208, 7.874)	0.258	0.760	0.891	46.831

4.1.2. Dual-source reconstruction

The reconstruction results of the dual-source experiment are presented in Fig. 4, and the corresponding quantitative evaluations are summarized in Table 3. From left to right, the columns correspond to FISTA, IVTCG, ReSL0, OMP-KSVD, and AOMP-GKSVD. The top row shows the 3D reconstructions, in which the reconstructed sources are highlighted in red, and the bottom row shows the corresponding cross-sectional views at the plane $X = -3$ *mm*, where the true target

Optics EXPRESS

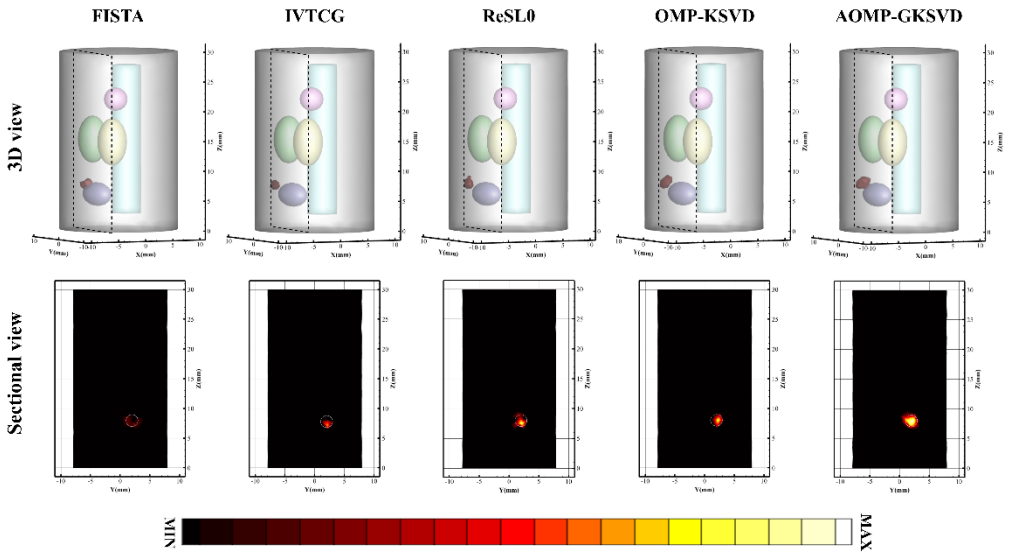

Fig. 3. Reconstruction results of five methods for the single-source numerical simulation.

Table 3. Quantitative results of different methods in dual-target reconstruction experiment.

Method	Reconstructed results (*mm*)	LE (*mm*)	Total LE (*mm*)	DICE	CNR	Time (*s*)
FISTA-L_1	(−3.587, −8.396, 8.337)	1.523	2.964	0.145	0.119	137.316
	(−3.724, −7.993, 14.248)	1.441		0.265		
IVTCG-L_1	(−2.807, −7.605, 8.363)	0.650	1.267	0.596	0.201	87.705
	(−2.854, −6.731, 14.464)	0.617		0.532		
ReSL0	(−3.179, −7.431, 8.208)	0.550	1.089	0.475	0.237	89.519
	(−3.190, −7.018, 15.505)	0.539		0.329		
OMP-KSVD	(−3.148, −7.424, 8.270)	0.504	0.976	0.596	0.379	90.197
	(−3.192, −6.986, 15.432)	0.472		0.599		
AOMP-GKSVD	(−2.781, −7.401, 8.477)	0.458	0.838	0.800	0.543	88.486
	(−3.069, −6.662, 15.160)	0.380		0.804		

Optics EXPRESS

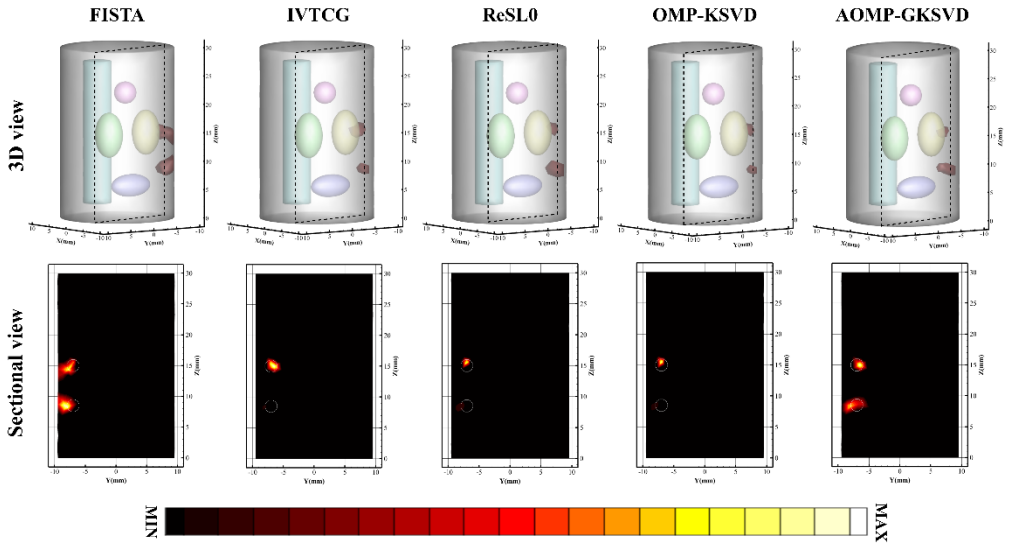

Fig. 4. Reconstruction results of five methods for the dual-source numerical simulation.

positions are outlined by white circles. Among the five algorithms, AOMP-GKSVD successfully resolves both sources with the highest fidelity, achieving the most accurate localization and the highest spatial overlap with the ground truth. Quantitatively, AOMP-GKSVD achieves the lowest total LE of 0.838 *mm* and the highest DICE values of 0.800 and 0.804 for the two sources, together with the highest CNR of 0.543. In contrast, FISTA exhibits significant localization deviations and poor spatial overlap, while IVTCG, ReSL0, and OMP-KSVD achieve improved localization performance relative to FISTA but remain limited in morphological recovery and contrast-to-noise performance. In addition, AOMP-GKSVD is slightly faster than OMP-KSVD and ReSL0, while remaining comparable to IVTCG and substantially faster than FISTA. These results demonstrate that AOMP-GKSVD provides superior accuracy and robustness in reconstructing multiple, spatially distinct bioluminescent sources.

4.1.3. Robustness to noise

Figure 5 illustrates the noise robustness of the AOMP-GKSVD algorithm under Gaussian noise levels ranging from 5% to 30%. The algorithm exhibits remarkable stability across all noise intensities, with the LE consistently maintained within a narrow range of 0.253 *mm* to 0.267 *mm* and the DICE fluctuating minimally between 0.740 and 0.760. These results indicate that the proposed method preserves high localization accuracy and reliable morphological recovery even in the presence of significant noise, demonstrating strong robustness to measurement noise.

4.2. Light source implantation experiment results

The feasibility of the AOMP-GKSVD method was validated through an *in vivo* experiment using a mouse with an implanted light source. As shown in Fig. 6, the 3D reconstruction results obtained by the five methods are presented in the top row, with the corresponding axial slices at the plane $Z = 20$ *mm* shown in the bottom row. In both views, the reconstructed light source is highlighted in red, and the true location and boundary of the implanted target are indicated by a white circle. Quantitative evaluation of the reconstruction performance is summarized in Table 4. Among the five methods, AOMP-GKSVD achieves the lowest LE of 0.395 *mm*, the highest DICE of 0.723, and the highest CNR of 0.128, indicating superior localization accuracy, morphological recovery, and contrast-to-noise performance. In contrast, FISTA and IVTCG yield larger LE

Optics EXPRESS

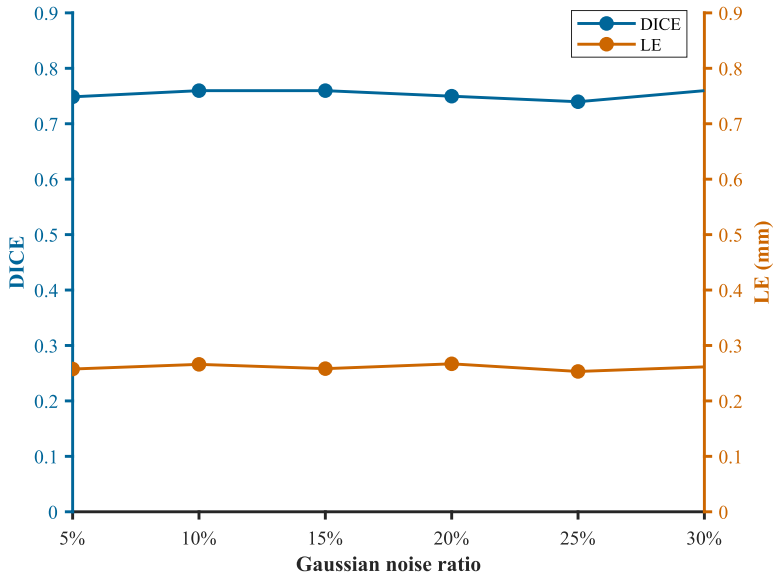

Fig. 5. Noise robustness of the AOMP-GKSVD algorithm under different Gaussian noise levels.

values of 1.558 *mm* and 0.765 *mm* and lower DICE values of 0.138 and 0.362, respectively, and their CNR values are 0.001 and 0.070. ReSL0 and OMP-KSVD provide moderate performance, with LE values of 0.723 *mm* and 0.628 *mm*, DICE values of 0.584 and 0.563, and CNR values of 0.091 and 0.097, yet both ReSL0 and OMP-KSVD remain inferior to AOMP-GKSVD in terms of localization accuracy, morphological recovery, and contrast-to-noise performance. In addition, AOMP-GKSVD achieves a slightly shorter runtime than ReSL0 and OMP-KSVD, while remaining comparable to IVTCG and markedly faster than FISTA. These results confirm that AOMP-GKSVD provides the most reliable reconstruction of the implanted light source, achieving both precise localization and accurate shape recovery.

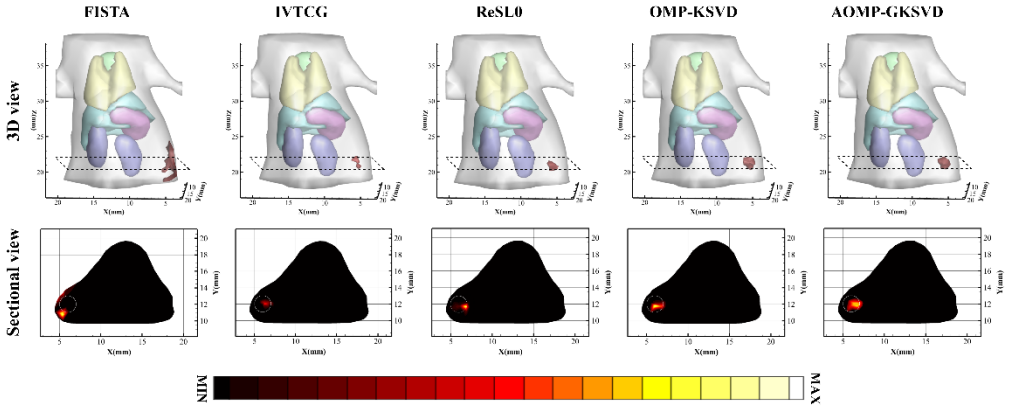

Fig. 6. Reconstruction results of *in vivo* light source implantation experiment.

Optics EXPRESS

Table 4. Quantitative results of *in vivo* light source implantation experiment.

Method	Reconstructed results (*mm*)	LE (*mm*)	DICE	CNR	Time (*s*)
FISTA-L_1	(4.896, 11.207, 19.237)	1.558	0.138	0.001	199.254
IVTCG-L_1	(6.736, 12.047, 20.201)	0.765	0.362	0.070	141.598
ReSL0	(6.603, 11.726, 19.709)	0.723	0.584	0.091	152.682
OMP-KSVD	(6.070, 11.652, 19.481)	0.628	0.563	0.097	155.445
AOMP-GKSVD	(6.333, 11.847, 19.853)	0.395	0.723	0.128	147.633

5. Discussion and conclusion

BLT is a powerful and non-invasive imaging modality with high sensitivity, showing significant potential for preclinical optical molecular imaging. However, BLT reconstruction remains a severely ill-posed inverse problem, making it highly sensitive to noise and measurement errors, which often leads to unstable source localization and inaccurate morphological recovery. Traditional iterative algorithms often suffer from slow convergence, suboptimal solutions, and limited robustness, whereas dictionary learning-based approaches, though more flexible, substantially increase computational complexity due to the iterative sparse coding and dictionary updates.

To address these challenges, we developed the AOMP-GKSVD method, a believed to be novel framework that integrates adaptive sparse coding with a structure-aware, group-based dictionary update strategy. In the sparse coding stage, adaptive sparsity estimation is incorporated into the OMP framework, allowing the sparsity level to be automatically determined from the measurement data and the system matrix. This eliminates the need for empirically tuned sparsity parameters and enables a more accurate and faithful representation of the underlying source distribution. In the dictionary update stage, a group-based strategy is employed based on the tetrahedral mesh structure, where adjacent nodes form overlapping groups and the corresponding dictionary atoms are optimized collectively. This strategy effectively leverages local spatial priors, promoting the reconstruction of clustered sources that are morphologically consistent with biological reality and improving computational efficiency.

The superior performance of the AOMP-GKSVD algorithm was systematically validated through numerical simulations and an *in vivo* light source implantation experiment. In both single- and dual-source simulations, AOMP-GKSVD consistently outperformed representative algorithms, including FISTA, IVTCG, ReSL0, and OMP-KSVD, in terms of localization accuracy, morphological recovery, and contrast-to-noise performance. In the single-source case, it achieved the lowest LE of 0.258 *mm*, the highest DICE of 0.760, and the highest CNR of 0.891. In the dual-source case, AOMP-GKSVD successfully resolved two closely positioned targets, demonstrating strong spatial discrimination capability, with the lowest total LE of 0.838 *mm*, the highest DICE values of 0.800 and 0.804, and the highest CNR of 0.543. Robustness was further validated in anti-noise experiments, where localization errors remained within 0.253 *mm* to 0.267 *mm* even under noise levels up to 30%. In the *in vivo* implantation experiment, AOMP-GKSVD provided accurate source localization with an LE of 0.395 *mm*, strong morphological fidelity with a DICE of 0.723, and improved contrast-to-noise performance with a CNR of 0.128. In addition, the computational times reported in the quantitative tables indicate that AOMP-GKSVD remains computationally competitive across diverse experimental settings. These results collectively demonstrate the effectiveness and robustness of AOMP-GKSVD under both simulated and practical conditions.

Despite its demonstrated advantages, several limitations remain. The generalizability of the AOMP-GKSVD framework requires further validation across different optical imaging modalities and in more complex biological models that better replicate clinical conditions. Future work will

Optics EXPRESS

therefore focus on extending this proposed methodology to other tomographic techniques and conducting comprehensive *in vivo* studies to further confirm its robustness and practical utility in diverse research settings.

In summary, this study introduces AOMP-GKSVD, a robust reconstruction framework for BLT. By synergistically combining adaptive sparsity estimation with a group-structured dictionary learning strategy, the proposed algorithm achieves superior localization accuracy, morphological recovery, and contrast-to-noise performance compared with existing methods. These findings demonstrate the potential of AOMP-GKSVD to enhance the reliability and practical applicability of BLT in preclinical molecular imaging and provide a solid foundation for its future extension to broader biomedical research contexts.

Funding. National Major Scientific Research Instrument Development Projects of China (82127805); Key Research and Development Program of Shaanxi Province (2024SF-YBXM-681); National Natural Science Foundation of China (61701403, 61806164).

Disclosures. The authors declare no conflicts of interest.

Data availability. Data underlying the results presented in this paper are not publicly available at this time but may be obtained from the authors upon request.

References

1. H. Guo, Z. Hu, X. He, *et al.*, "Non-convex sparse regularization approach framework for high multiple-source resolution in Cerenkov luminescence tomography," Opt. Express **25**(23), 28068–28085 (2017).
2. Y. Liu, M. Chu, H. Guo, *et al.*, "Multispectral differential reconstruction strategy for bioluminescence tomography," Front. Oncol. **12**, 768137 (2022).
3. C. Qin, J. Zhong, Z. Hu, *et al.*, "Recent advances in Cerenkov luminescence and tomography imaging," IEEE J. Sel. Top. Quantum Electron. **18**(3), 1084–1093 (2012).
4. S. Ren, L. Wang, Q. Zeng, *et al.*, "Effective reconstruction of bioluminescence tomography based on GPU-accelerated inverse Monte Carlo method," AIP Adv. **10**(10), 105329 (2020).
5. Q. Zhang, H. Zhao, D. Chen, *et al.*, "Source sparsity based primal-dual interior-point method for three-dimensional bioluminescence tomography," Opt. Commun. **284**(24), 5871–5876 (2011).
6. H. Guo, J. Yu, Z. Hu, *et al.*, "A hybrid clustering algorithm for multiple-source resolving in bioluminescence tomography," J. Biophotonics **11**(4), e201700056 (2018).
7. H. Guo, L. Gao, J. Yu, *et al.*, "Sparse-graph manifold learning method for bioluminescence tomography," J. Biophotonics **13**(4), e201960218 (2020).
8. D. Yang, L. Wang, D. Chen, *et al.*, "Filtered maximum likelihood expectation maximization based global reconstruction for bioluminescence tomography," Med. Biol. Eng. Comput. **56**(11), 2067–2081 (2018).
9. Y. Gao, K. Wang, S. Jiang, *et al.*, "Bioluminescence tomography based on Gaussian weighted Laplace prior regularization for *in vivo* morphological imaging of glioma," IEEE Trans. Med. Imaging **36**(11), 2343–2354 (2017).
10. N. Hartung, S. Mollard, D. Barbolosi, *et al.*, "Mathematical modeling of tumor growth and metastatic spreading: validation in tumor-bearing mice," Cancer Res. **74**(22), 6397–6407 (2014).
11. M. Chehade, A. K. Srivastava, and J. W. M. Bulte, "Co-registration of bioluminescence tomography, computed tomography, and magnetic resonance imaging for multimodal *in vivo* stem cell tracking," Tomography **2**(2), 158–165 (2016).
12. J. Feng, K. Jia, Z. Li, *et al.*, "Bayesian sparse-based reconstruction in bioluminescence tomography improves localization accuracy and reduces computational time," J. Biophotonics **11**(4), e201700214 (2018).
13. X. Zhang, Y. Lu, and T. Chan, "A novel sparsity reconstruction method from Poisson data for 3D bioluminescence tomography," J. Sci. Comput. **50**(3), 519–535 (2012).
14. X. He, J. Liang, X. Wang, *et al.*, "Sparse reconstruction for quantitative bioluminescence tomography based on the incomplete variables truncated conjugate gradient method," Opt. Express **18**(24), 24825–24841 (2010).
15. Y. Zhu, A. K. Jha, D. F. Wong, *et al.*, "Image reconstruction in fluorescence molecular tomography with sparsity-initialized maximum-likelihood expectation maximization," Biomed. Opt. Express **9**(7), 3106–3121 (2018).
16. H. Liu, X. Yang, T. Song, *et al.*, "Multispectral hybrid Cerenkov luminescence tomography based on the finite element SPn method," J. Biomed. Opt. **20**(8), 086007 (2015).
17. H. Shan, A. Padole, F. Homayounieh, *et al.*, "Competitive performance of a modularized deep neural network compared to commercial algorithms for low-dose CT image reconstruction," Nat. Mach. Intell. **1**(6), 269–276 (2019).
18. B. Rezaeifar, C. J. A. Wolfs, N. G. Lieuwes, *et al.*, "A deep-learning assisted bioluminescence tomography method to enable radiation targeting in rat glioblastoma," Phys. Med. Biol. **68**(15), 155013 (2023).
19. G. Ongie, A. Jalal, C. A. Metzler, *et al.*, "Deep learning techniques for inverse problems in imaging," IEEE J. Sel. Areas Inf. Theory **1**(1), 39–56 (2020).
20. H. Chen, K. Shou, S. Chen, *et al.*, "Smart self-assembly amphiphilic cyclopeptide-dye for near-infrared window-II imaging," Adv. Mater. **33**(16), 2006902 (2021).
21. N. Cao, A. Nehorai, and M. Jacob, "Image reconstruction for diffuse optical tomography using sparsity regularization and expectation-maximization algorithm," Opt. Express **15**(21), 13695–13708 (2007).

Optics EXPRESS

22. Z. Hu, M. Zhao, Y. Qu, *et al.*, "In vivo 3-dimensional radiopharmaceutical-excited fluorescence tomography," J. Nucl. Med. **58**(1), 169–174 (2017).
23. J. Fan and R. Li, "Variable selection via nonconcave penalized likelihood and its oracle properties," J. Am. Stat. Assoc. **96**(456), 1348–1360 (2001).
24. C H. Zhang, Nearly unbiased variable selection under minimax concave penalty. 2010.
25. S. R. Arridge and J. C. Schotland, "Optical tomography: forward and inverse problems," Inverse Problems **25**(12), 123010 (2009).
26. D. Calvetti and E. Somersalo, "Inverse problems: From regularization to Bayesian inference," WIREs Computational Stats. **10**(3), e1427 (2018).
27. J. Feng, K. Jia, C. Qin, *et al.*, "Three-dimensional bioluminescence tomography based on Bayesian approach," Opt. Express **17**(19), 16834–16848 (2009).
28. I. Y. Chun and J. A. Fessler, "Convolutional dictionary learning: Acceleration and convergence," IEEE Trans. on Image Process. **27**(4), 1697–1712 (2018).
29. S. Boyd, N. Parikh, E. Chu, *et al.*, "Distributed optimization and statistical learning via the alternating direction method of multipliers," FNT in Machine Learning **3**(1), 1–122 (2010).
30. A. Beck and M. Teboulle, "A fast iterative shrinkage-thresholding algorithm for linear inverse problems," SIAM J. Imaging Sci. **2**(1), 183–202 (2009).
31. J. Wang and B. Shim, "On the recovery limit of sparse signals using orthogonal matching pursuit," IEEE Trans. Signal Process. **60**(9), 4973–4976 (2012).
32. L. Kong, Y. An, Q. Liang, *et al.*, "Reconstruction for fluorescence molecular tomography via adaptive group orthogonal matching pursuit," IEEE Trans. Biomed. Eng. **67**(9), 2518–2529 (2020).
33. S. Li, L. Fang, and H. Yin, "An efficient dictionary learning algorithm and its application to 3-D medical image denoising," IEEE Trans. Biomed. Eng. **59**(2), 417–427 (2012).
34. M. Ju, T. Han, R. Yang, *et al.*, "An adaptive sparsity estimation KSVD dictionary construction method for compressed sensing of transient signal," Math. Probl. Eng. **2022**(1), 1–12 (2022).
35. L. Su, L. Chen, W. Tang, *et al.*, "Dictionary Learning Method Based on K-Sparse Approximation and Orthogonal Procrustes Analysis for Reconstruction in Bioluminescence Tomography," J. Biophotonics **17**(11), e202400308 (2024).
36. M. Aharon, M. Elad, and A. Bruckstein, "K-SVD: An algorithm for designing overcomplete dictionaries for sparse representation," IEEE Trans. Signal Process. **54**(11), 4311–4322 (2006).
37. S. Jiang, J. Liu, Y. An, *et al.*, "Fluorescence molecular tomography based on group sparsity priori for morphological reconstruction of glioma," IEEE Trans. Biomed. Eng. **67**(5), 1429–1437 (2020).
38. L. Yin, K. Wang, T. Tong, *et al.*, "Adaptive grouping block sparse Bayesian learning method for accurate and robust reconstruction in bioluminescence tomography," IEEE Trans. Biomed. Eng. **68**(11), 3388–3398 (2021).
39. H. Bu, R. Tao, X. Bai, *et al.*, "Regularized smoothed $\ell 0$ norm algorithm and its application to CS-based radar imaging.," Signal Processing **122**, 115–122 (2016).
40. A. D. Klose, V. Ntziachristos, and A. H. Hielscher, "The inverse source problem based on the radiative transfer equation in optical molecular imaging," J. Comput. Phys. **202**(1), 323–345 (2005).
41. A. D. Klose and E. W. Larsen, "Light transport in biological tissue based on the simplified spherical harmonics equations," J. Comput. Phys. **220**(1), 441–470 (2006).
42. W. Yang, W. Qin, Z. Hu, *et al.*, "Comparison of Cerenkov luminescence imaging (CLI) and gamma camera imaging for visualization of let-7 expression in lung adenocarcinoma A549 Cells," Nuclear Medicine and Biology **39**(7), 948–953 (2012).
43. G. Gasso, A. Rakotomamonjy, and S. Canu, "Recovering sparse signals with a certain family of nonconvex penalties and DC programming," IEEE Trans. Signal Process. **57**(12), 4686–4698 (2009).
44. Y. Liu, H. Guo, H. Zhao, *et al.*, "A finite element mesh regrouping-based hybrid light transport model for enhancing the efficiency and accuracy in bioluminescence tomography," *Medical Imaging 2020: Physics of Medical Imaging*. SPIE, 2020, 11312: 584–593.
45. G. Zhang, J. Zhang, Y. Chen, *et al.*, "Logarithmic total variation regularization via preconditioned conjugate gradient method for sparse reconstruction of bioluminescence tomography," Computer Methods and Programs in Biomedicine **243**, 107863 (2024).
46. B. Parvitte, C. Risser, R. Vallon, *et al.*, "Quantitative simulation of photoacoustic signals using finite element modelling software," Appl. Phys. B **111**(3), 383–389 (2013).
47. N. Ren, J. Liang, X. Qu, *et al.*, "GPU-based Monte Carlo simulation for light propagation in complex heterogeneous tissues," Opt. Express **18**(7), 6811–6823 (2010).